Electronic Supplementary Material (ESI) for Nanoscale.
This journal is © The Royal Society of Chemistry 2018

Nanoscale

Ultra-strong nanotwinned Al-Ni solid solution alloy with significant plasticity

*Y.F. Zhang[a], Q. Li[a], S, Xue[a], Jie Ding[a], D.Y. Xie[c], Jin Li[a], Han Wang[a], Haiyan Wang [a,b], J. Wang[c] and X. Zhang[a]**

[a] *School of Materials Engineering, Purdue University, West Lafayette, IN 47907, United States*
[b] *School of Electrical and Computer Engineering, Purdue University, West Lafayette, IN 47907,*
[c] *Mechanical and Materials Engineering, University of Nebraska-Lincoln, Lincoln, NE 68588*

S1. Microstructure Characterization (Figs. S1-S5)

S2. Measurements and Mechanisms of local deformation (Figs. S6-S9)

S3. First-principles density function theory calculations

S1. Microstructure Characterization.

The d spacing of out-of-plane (111) was calculated by using Bragg's law, given the peak position of Al (111). The same peak position of Si (111) at different Ni compositions indicates the reliability of each XRD measurement. Fig. S1a shows the dependence of out-of-plane {111} d spacing on the Ni composition. d spacing keeps relatively constant at 6.1 at% Ni or less, while increase monotonically with Ni composition. We ascribe such trend to the internal stresses induced by the Ni solutes. The enlarged out-of-plane (111) spacing proves the compressive in-plane stress. Smaller Ni solute atoms preferentially reside in substitutional site based on our DFT calculations (in section S3), which can partially counterbalance the accumulation of in-plane stress at low Ni composition (<6.1at.%). At high Ni composition, excess Ni solute atoms tend to locate at interstitial sites, resulting in larger {111} d spacing. In addition, smaller column size (more column boundaries) with higher fraction of free volumes and vacancies might give rise to higher compressive stress, and thus larger d value. The peak intensity ratio of Al (111)/Si (111) was calculated based on the collected peak counts of Al (111) and Si (111) respectively. As shown in Fig. S1(b), the relative peak intensity of Al (111) grows with Ni content. This result further

confirms that the addition of Ni solutes can enhance the Al (111) texture, which is consistent with our TEM analysis.

Plan-view and dark field cross-section TEM micrographs (Fig. S2) illustrate the microstructure evolution of Al-Ni alloys. At 4.5 at% Ni or less, Al-Ni films have polycrystalline columnar grains. In comparison, higher Ni composition (>6.1%) leads to the formation of highly-twinned nano columns. Interestingly, the grain size of theses nano columns slightly decrease from the film free surface to the film- substrate interface.

Statistics of grain size were performed based on these plan-view or cross-section TEM images. More than 200 grains were measured by using digital micrograph to ensure the reliability of data. Apart from obvious grain size reduction, statistics also show growing twin density with increasing Ni composition(Fig. S5).

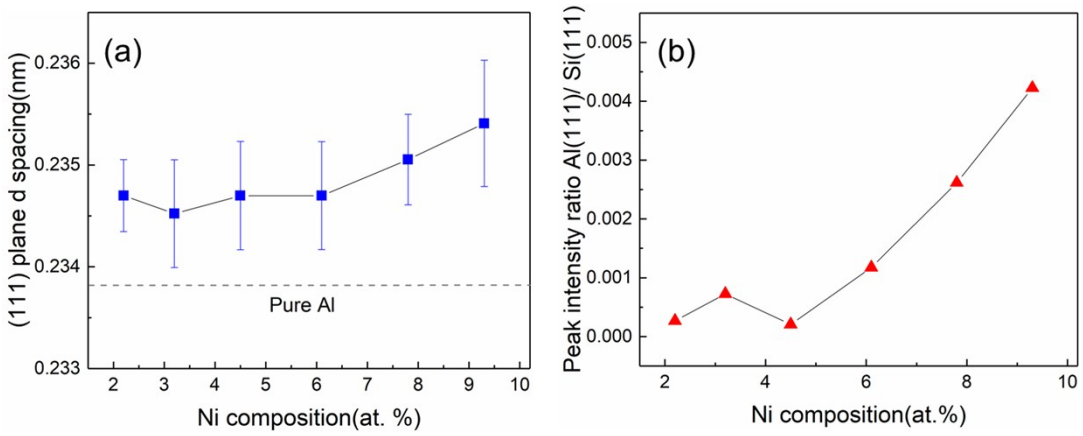

Fig.S1. (a) The d spacing of out-of-plane {111} plane of Al-Ni alloys with different Ni composition. (b) Variation of Al (111)/ Si (111) peak intensity ratio with the Ni composition.

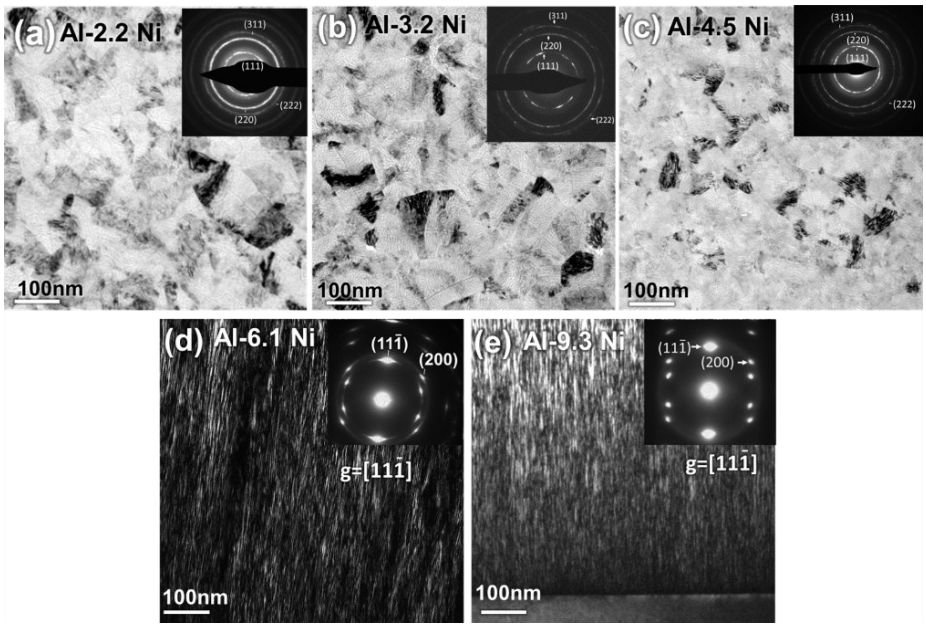

Fig.S2. (a-c) Plan-view TEM micrographs and corresponding SAD patterns of Al-2.2Ni, Al-3.2 Ni and Al-4.5Ni show polycrystalline grains. (d-e) Dark-field cross-section TEM images and the inserted SAD patterns of Al-6.1Ni and Al-9.3Ni demonstrate the nanotwinned columns with {111} texture

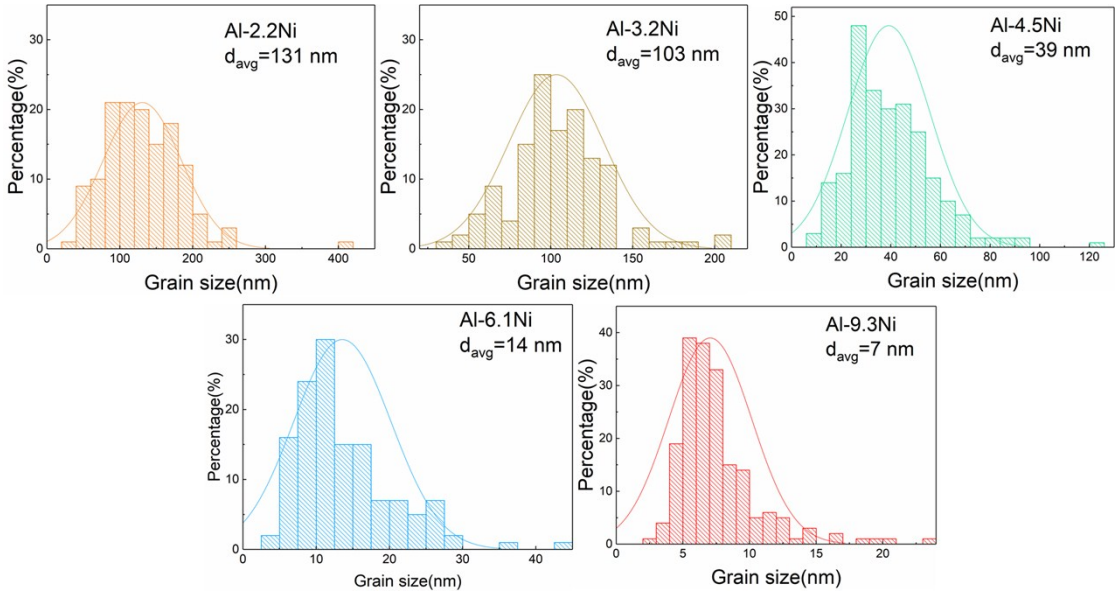

Fig.S3. The statistics of grain size distributions of Al-Ni alloys shows the reduction of average grain sizes with the increasing Ni composition.

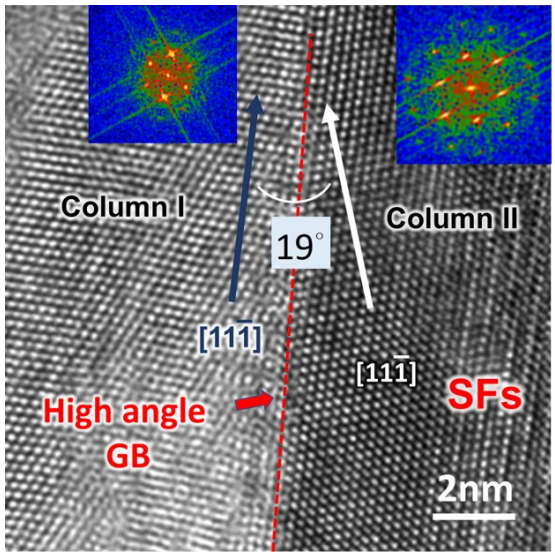

Fig. S4 Bright-field cross section TEM image shows the high-angle grain boundary in Al-4.5Ni Approximately, the misorientation relation between the column I and column II is {111}||{112}

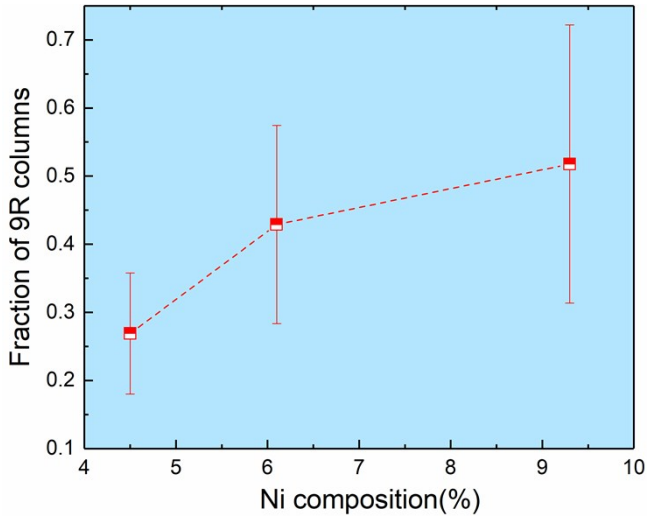

Fig. S5. The fraction of columns with 9R at different Ni compositions

S2. Measurement of local deformation

Real-time diameters were recorded at two different positions (Fig. S6a) on the pillar as a function of displacement (Fig. S6 b-c). Subsequently, the in-plane and out-of-plane strains were calculated and plotted against pillar height respectively (Fig S6 d-e) based on instantaneous diameters. The in-plane strain decreases from top to the bottom along the pillar height, and the plasticity is mainly accommodated by the top of the pillar. Post-compression TEM analysis demonstrates the grain coarsening, grain rotation and detwinning in the top region of the pillar. SAD patterns taken from three different regions (Fig. S7) on the pillar also show the graduate grain

rotation along the pillar height. Thus, plasticity is mainly accommodated by grain rotation, coalescence and detwinning initiating from the pillar top. These processes involve ITBs migration and glide of partial dislocations, leaving behind ITB retentions and nanotwins in the deformed zone (Fig. S8), as schematized in Fig. S8. In {111}-textured films like Al-9.3 Ni, there is little resolved shear stress in to driven glide of partial dislocations, while polycrystalline films (e.g. Al-4.5Ni) have slip planes with larger Schmid factor. This might explain the significant difference of flow stress between Al-9.3Ni and Al-4.5Ni. In general, the combination of strain softening on the top and strain hardening in the pillar bottom gives rise to the high strength of Al-Ni during the pillar compression tests. More details can be found in the main text.

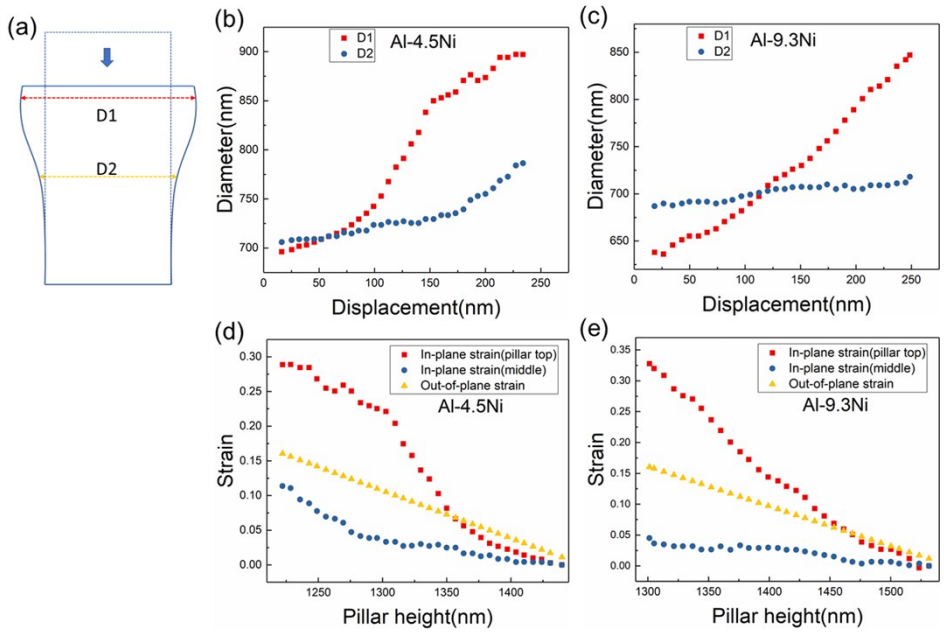

Fig. S6. Instantaneous pillar diameter changes at different portions measured during *in situ* micropillar compression experiments in the SEM microscope. (a) A schematic diagram showing the location where real-time diameters are recorded. (b) A representative example of the diameter changes of compressed Al-4.5Ni pillar; D1 is the diameter of the pillar top, and D2 is the mid-height pillar diameter. (c) The evolution of pillar diameter during compression of the Al-9.3Ni specimen; Plot of in-plane and out-of-plane strain at different pillar heights for Al-4.5Ni(d) and Al-9.3Ni(e).

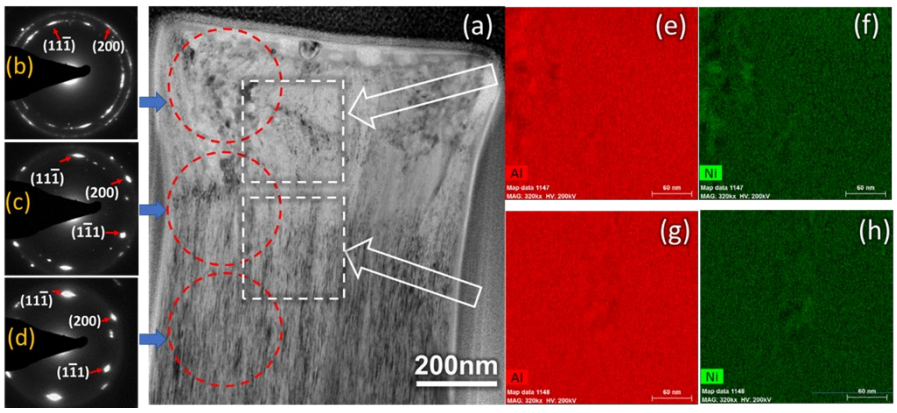

Fig. S7. (a) Low-magnification XTEM micrograph of the deformed Al-9.3Ni pillar with corresponding SADs (b-d), and EDX composition mapping (e-h). (b-d) SADs taken from the pillar top, medium and bottom demonstrate the deformation induced prominent grain rotation in the top portion of the pillar. (e-h) EDX analyses reveal relatively uniformly distributed Ni solutes near the top and the middle portions of the deformed pillar.

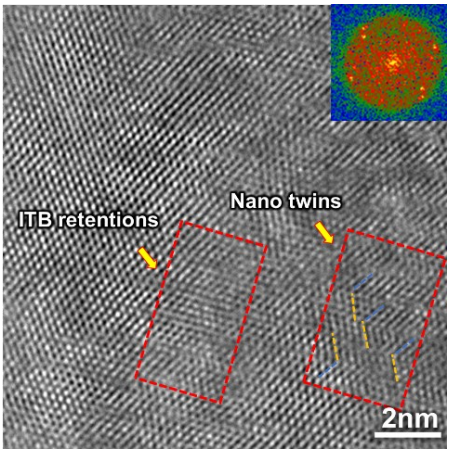

Fig. S8. High-resolution TEM (HRTEM) image examined from <110> zone axis shows the retention of ITBs and nanotwins near the top of the deformed Al-9.3Ni pillar.

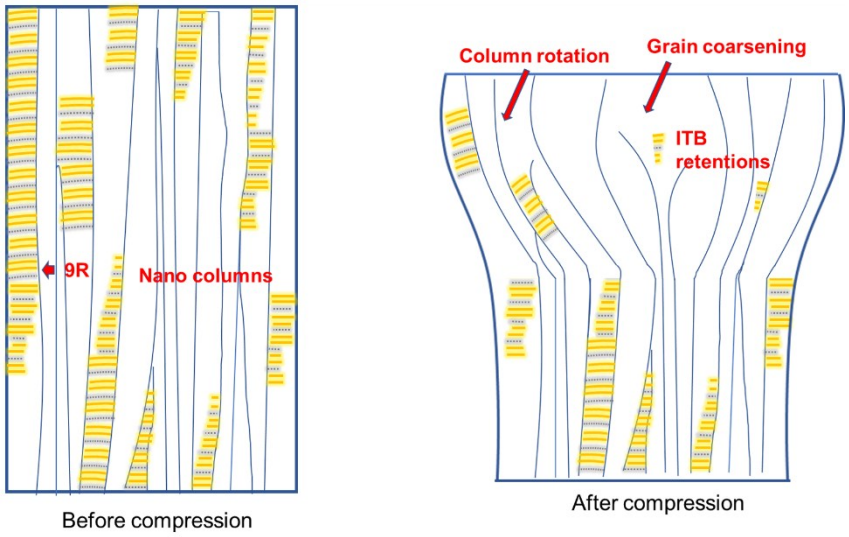

Fig. S9. Schematics showing the microstructure evolution of the nanotwinned Al-Ni alloys before and after compression. Column boundary migration, grain coarsening and detwinning take place on the deformed pillar top, in comparison to the highly-twinned nanocolumns before compression.

S3. DFT calculations

The Vienna ab-initio simulation package (VASP) was employed to conduct density functional theory (DFT) calculations. Atomic relaxations and calculations of total energies are performed with projector augmented wave (PAW) method [1] and generalized gradient approximation (GGA) approach [2]. Perdew-Burke-Ernzerhof (PBE) exchange-correlation density functionals [3] were used during the computation. For Aluminum and Nickel, the pseudopotentials were constructed using electron configurations of s2p1 and d8s2 respectively [4]. A 500-eV cut-off on kinetic energy was used for the plane waves basis set. The first Brillouin zone of Aluminum and Nickel unit cell were sampled by 12×12×12 Monkhorst–Pack k-point grid [5]. The self-consistent iteration was stopped, when the change of total energy is smaller than 10-5 eV. The convergence criteria of geometry optimizations are that the forces acting on each atom is smaller than 0.01eV/Å. For aluminum with FCC structure, the calculated lattice parameter is 4.037 Å and the cohesive energy is 3.50eV. For nickel with FCC structure, the calculated lattice parameter is 3.518 Å and the cohesive energy is 4.92eV.

As shown in Fig. S7, the Nickel solute is evenly dispersed in the matrix and significantly increases the density and stability of twin boundaries and stacking faults. To understand the origin

of this phenomenon, the DFT calculations were used to evaluate the formation energy of Nickel solute atoms and the effect of solute atoms on stacking faults

To calculate the formation energies of Nickel solute atoms, the unit cell of aluminum was repeated in three <100> directions and formed a 3×3×3 supercell, which contains 108 atoms. And a 4×4×4 M–P k-point grid is used in this part of calculation. After adding or substituting Nickel atom in this model, we can calculate the formation energy of Nickel solute atoms. The formation energy of an individual substitutional Nickel atom is -0.940 eV. For the Nickel atoms located at tetrahedral and octahedral site, the formation energy is 1.601eV and 0.058eV. The lower formation energy of substitutional atom indicates that the solute atoms can stably stay at substitutional sites. The minus value shows that the bonding between Al and Ni is quite strong, which consist with the fact that these two elements can form thermodynamically stable intermetallic. In order to know the tendency of segregation of Nickel, the formation energies of Nickel substitutional atom pairs are computed. For pairs of substitution atoms that are located at the first, second, third, and forth nearest positions, the formation energy per atom are -0.644 eV, -0.593 eV, -0.592 eV, and -0.544 eV. The closer atoms locate, the lower formation energy they will have. But the formation energy of 4 nearest solute atoms is -0.274 eV per atom. This relatively high value means the segregation of solute atoms are not thermodynamically performed. This result is confirmed by EDX mapping of the specimen, which suggests the solute atoms are uniformly distributed.

To find the reason why Nickel can induce large number of twins and stacking faults, firstly, we analyzed the influence of solute atoms on stacking fault energy(SFE). In this process, the stacking fault energies of aluminum with and without solute atoms on fault plane were calculated. Calculations of SFEs were performed with slab models, as shown in figure 1.a, containing 8 layers of FCC (111) plane. There are 16 atoms in each layer. The first Brillouin zone was integrated by 9×9×3 M-P K points. The computed stacking fault energy of pure aluminum is 119.9 mJ/m2, which consists with experimental stacking fault energy 120-144 mJ/m2 [6,7]. The SFE with Ni solute atoms is 111.8 mJ/m2. The Nickel atoms on the fault planes can lower the SFE, thus increase the number of twins and stacking faults.

In the next step, to know how difficult it is to annihilate stacking fault and de-twin, generalized stacking fault energies are calculate using surface trimer and heptamer, as shown in figure 1.b. Two atomic layers of {111} Al are used as substrate in the x-y plane. Each monolayer

contains 16 and 36 atoms for trimer and heptamer. 6×6×3 and 3×3×3 M-P K points grids are used for trimer and heptamer model respectively. The bottom layer (A layer in figure1.c) is fixed, when calculating the energy of models with FCC stacking and faulted stacking. Then a chain of transient states is produced by linearly interpolating between models with FCC stacking and faulted stacking. The transient state models are relaxed while fixing the atoms in x-y plane (can only move along z direction). The excess energy per surface atom was obtained and plotted in figure 1.d. The stacking fault recovery energy barrier for pure aluminum heptamer and heptamer with Ni is 0.064eV and 0.089 eV. The energy barrier is dramatically increased by solute atom. Therefore, the nano-twin and stacking faults formed during vapor deposition is preserve in the sample.

References

[1] Blöchl, Peter E. "Projector augmented-wave method." Physical review B 50.24 (1994): 17953.

[2] Langreth, David C., and M. J. Mehl. "Beyond the local-density approximation in calculations of ground-state electronic properties." Physical Review B 28.4 (1983): 1809.

[3] Perdew, John P., Kieron Burke, and Matthias Ernzerhof. "Generalized gradient approximation made simple." Physical review letters 77.18 (1996): 3865.

[4] Kresse, Georg, and D. Joubert. "From ultrasoft pseudopotentials to the projector augmented-wave method." Physical Review B 59.3 (1999): 1758.

[5] Monkhorst, Hendrik J., and James D. Pack. "Special points for Brillouin-zone integrations." Physical review B 13.12 (1976): 5188.

[5] Westmacott, K. H., and R. L. Peck. "A rationalization of secondary defect structures in aluminium-based alloys." Philosophical Magazine 23.183 (1971): 611-622.

[6] Rautioaho, R. H. "An interatomic pair potential for aluminium calculation of stacking fault energy." physica status solidi (b) 112.1 (1982): 83-89.